



THE UNIVERSITY OF TEXAS AT ARLINGTON
DEPARTMENT OF MECHANICAL AND AEROSPACE ENGINEERING

MAE 3182: AERODYNAMICS AND FLUIDS LAB
FLOW OVER A CYLINDER

Fall 2023

INSTRUCTOR: Vijay Gopal, Ph.D.
TEACHING ASSISTANT: Sandeep Eldho James.

I. Learning Objectives

1. Analytical, experimental, and computational methods in incompressible aerodynamics.
2. Surface pressure measurements using a differential pressure scanner.
3. Data reduction and post-processing.
4. Drag estimation and wind tunnel correction.
5. Boundary layer separation analysis.
6. Practical applications of a data acquisition system (DAQ).
7. Computational fluid dynamics simulation tool.

II. Introduction

Flow over a circular cylinder has been widely studied in the literature. Both numerical and experimental investigation have been performed at various Reynolds numbers to capture different viscous flow characteristics. In this laboratory experiment, a two-dimensional circular cylinder in the subsonic wind tunnel crossflow is considered at low Reynolds number to study the surface pressure distribution, coefficient of drag and the location of flow separation at a given free-stream velocity. The main objective of this lab work is to understand the viscous flow characteristics for a cylinder in crossflow through an experiment and to compare the data with the results obtained from analytical and numerical methods.

The characteristics of fluid flow over a cylinder at different regimes of Reynolds number is first discussed. For the experiment in this lab work, a cylinder is designed with surface taps for wall pressure measurements. Since the flow over a cylinder is often associated with separation (i.e. boundary layer detachment), the surface pressure distribution differs from ideal inviscid predictions. A strong coupling between inviscid and viscous phenomena associated flow separation influences the prediction of drag force and the flow velocity distribution along the surface of the cylinder.

In this lab work, analytical relationship between surface pressure and flow velocity is established using Bernoulli equation with restricted assumptions. Using the surface pressure distribution, the pressure-drag on a cylinder is also investigated and compared with the literature data. A brief overview of an analytical method for boundary layer analysis is introduced here to predict the separation point. A computational fluid dynamic (CFD) tool is also introduced in this lab to provide a detailed insight in to flow characteristics and relevant fluid dynamic parameters for this study. The details of the experimental setup and procedure will be explained in this document.

The experimental data on the non-dimensionalized pressure profile will be compared with the CFD results and inviscid analytical results. The pressure drag evaluated from the experiments will be used to obtain the drag coefficient which will be compared with the CFD and the literature. Finally, a comparison of separation point location from experiment, CFD and the analytical method (explained in this document) will be part of the report requirements. The results obtained from this study can serve as the baseline for many other complex problems. For instance, the ideal flow over a cylinder can be easily extended to the flow over an airfoil using Joukowski's transformation.

III. Characteristics of Flow Over a Cylinder

Flow over a circular cylinder is vastly studied both experimentally and numerically. In this section a brief overview on different flow regimes based on Reynolds number is presented. Flow visualization techniques has revealed that at different Reynolds number, $Re_D = \rho_\infty U_\infty D / \mu_\infty$, the flow characteristics present different complex features, particularly in the aft part of the cylinder [1–6]. The complexity arises from the viscous effects that determines the position of the separation points along surface of the cylinder and the transition from laminar to turbulent flow. As the Reynolds number of the flow is increased, a laminar to turbulent flow regime is established. This transition doesn't take place in the entire flow field; however, the transition first takes place in the downstream wake region. Progressively as the Reynold number increases, the transition region moves closer to the cylinder. Finally, at very high Reynolds number, the boundary layer transition takes place in the forebody region of the cylinder. In this section only a brief description of different regimes is discussed that is summarized in a schematic (Fig. 1).

golf ball example:

pressure drag is the major contributor to total drag.

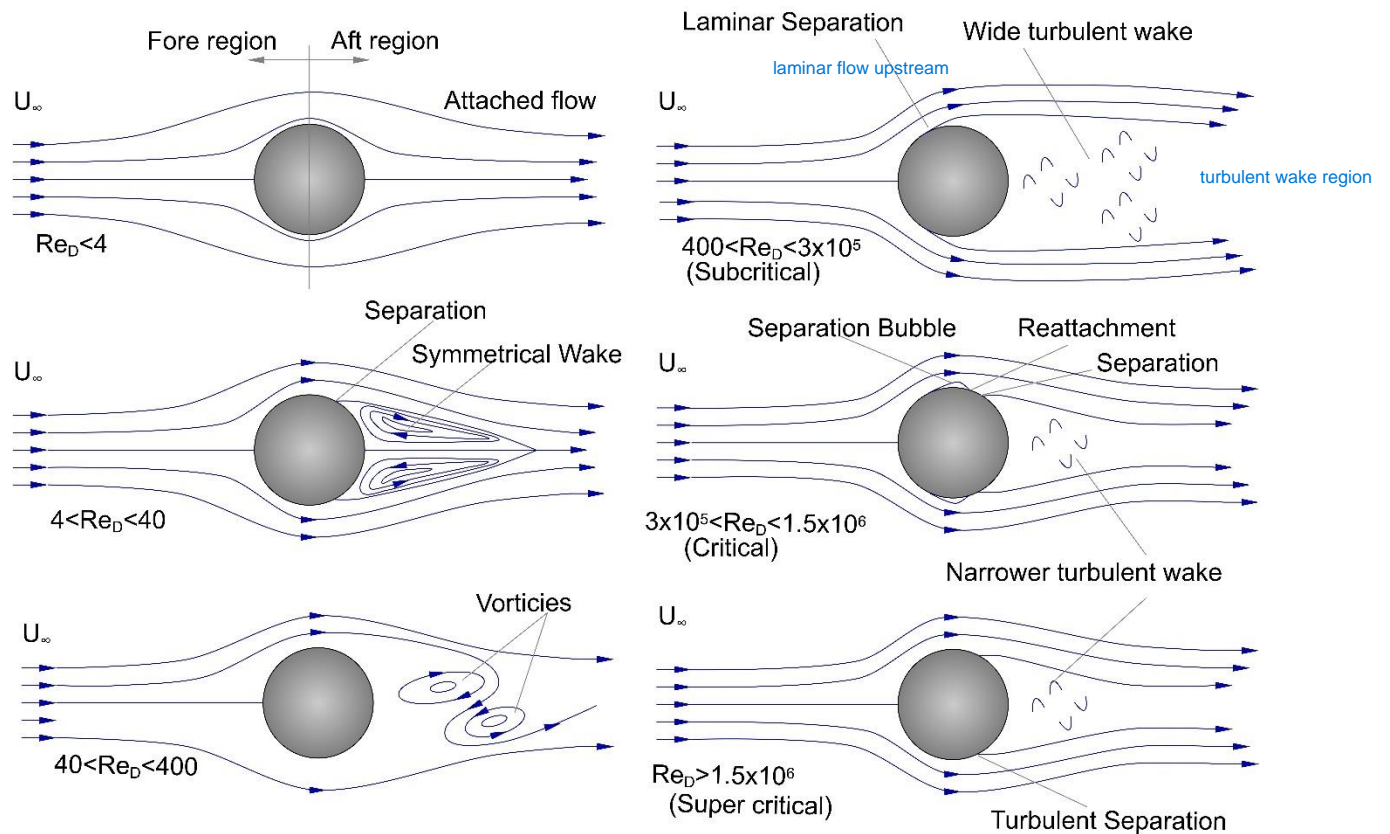


Figure 1: Schematic describing different flow regimes based on Reynold number Re_D .

Vortex shedding frequency.

When the free stream Reynolds number, $Re_D < 4$, is very low, the viscous boundary layer is attached across the entire circumference of the cylinder (Fig. 1). This regime is often referred to as stokes flow or creeping flow [6]. Since there is no separation, the pressure distribution is almost symmetrical and consequently a major portion of the drag force originates from the viscous boundary layer (i.e. skin friction) and the pressure drag contribution is comparatively smaller.

energized flow: small turbulences trip the flow in the boundary layer. There is momentum transfer, thereby energizing the flow.

As the Reynolds number increases, the flow separates from the cylinder circumference and a recirculating wake flow is established (Fig.1). Approximately between $4 < Re_D < 40$ the downstream length of the recirculating zone progressively increases while the flow is symmetrical and steady. Beyond $Re_D > 40$, the cylinder wake region becomes unsteady. While the wake is still laminar, it contains vortices that are periodically shed from both the sides of the cylinder in an alternate fashion. This causes fluctuating aerodynamic forces on the cylinder. The wake region in this regime is referred to as von Karman vortex street (Fig. 1). The vortex shed frequency, f , is usually reported in literature using a non-dimensional number that is referred to as Strouhal number, $St = fD/U_\infty$. The von Karman vortex street exist for a wide range of Reynolds number [6], specifically between $100 < Re_D < 10^5$, the downstream the Strouhal number remains fair constant at $St \approx 0.2$.

Increasing the Reynolds number beyond $Re_D > 400$, the turbulence in the wake region increases while the boundary-layer near and the separation points on the cylinder are still laminar. Also, with the increase in the Reynolds number the transition region in the wake region moves closer to the cylinder surface. In the range of $400 < Re_D < 3 \times 10^5$, laminar boundary layer separation occurs on the cylinder in the forebody region. The separation causes a wide downstream wake to develop. This regime is referred to as subcritical regime.

Further increase in the Reynolds number in the vicinity of 3×10^5 , the laminar boundary layer undergoes transition to turbulence immediately after laminar separation. This re-energizes the boundary layer and results in reattachment of the boundary layer. A separation bubble is then formed on the cylinder surface as shown in Fig. 1. The flow separates again in the turbulent regime in the aft part of the cylinder with a narrower wake downstream. The regime in which separation bubble is formed is referred to as the critical regime.

Beyond $Re_D > 1.5 \times 10^6$, the separation bubble disappears and the boundary layer flow in the forebody region of the cylinder becomes turbulent. This delays the separation point to the aft region causing a narrow turbulent wake to develop downstream. The regime, $Re_D > 1.5 \times 10^6$, is referred to as supercritical. A more detailed flow regime description is carried out in various literature [7] including some unstable regimes that are not discussed in this brief description. For the scope of the current lab work, different flow regimes as shown in Fig. 1 is summarized in Table 1.

Table 1: Summary of regimes in flow over a circular cylinder.

$Re_D = \rho_\infty U_\infty D / \mu_\infty$ Range	Flow Regime
0 – 4	Attached flow
4 – 40	Laminar symmetrical steady recirculating zone
40 – 400	Laminar flow with distinct vortex shedding
400 – 3×10^5	Subcritical (Laminar separation)
3×10^5 – 1.5×10^6	Critical (laminar separation bubble)
$> 1.5 \times 10^6$	Supercritical (Turbulent separation)

IV. Analytical Methods and Discussion

The aim of this section is to present some analytical tools for flow over a cylinder and to quantitatively determine the relevant fluid dynamic parameters. Particularly, discussion on surface pressure distribution, boundary layer edge velocity distribution, drag force and boundary layer separation point are discussed. Typical trends from literature are also discussed to serve as a guide to interpret the experimental data produced in this lab work.

A. Surface Pressure and Edge Velocity Distribution

For discussing the analytical study, consider the following schematic (Fig. 2) of viscous flow over a circular cylinder. The cartesian reference frame is taken to be $X - Y$ with its center at axis of the cylinder, the polar co-ordinate system is represented by $r - \theta$ and the curvilinear co-ordinate system is taken to be $r - x$. To solve a problem, any one of the reference frames is sufficient. However, multiple reference frames are introduced here for convenience. Using the polar co-ordinate system, any point in the flow field (like the point, p, in Fig. 2) is located at a radial distance r and at an angle θ . Note that the angle θ is measured from the cartesian X -axis in the clockwise direction. In the $r - x$ co-ordinate system, x represents the arc-length from the stagnation point to the desired location on the surface of the circular cylinder. At any given arbitrary point, p, the velocity can be resolved in the polar co-ordinates as v_θ and v_r along the unit vectors $\hat{\theta}$ and \hat{r} respectively. The boundary layer thickness, δ , varies along x which represents the demarcation between the inviscid region and the viscous dominated region. The flow field outside the boundary layer can be approximated to be irrotational or $\nabla \times \vec{V} \approx 0$ and the flow inside the boundary layer is rotational $\nabla \times \vec{V} \neq 0$.

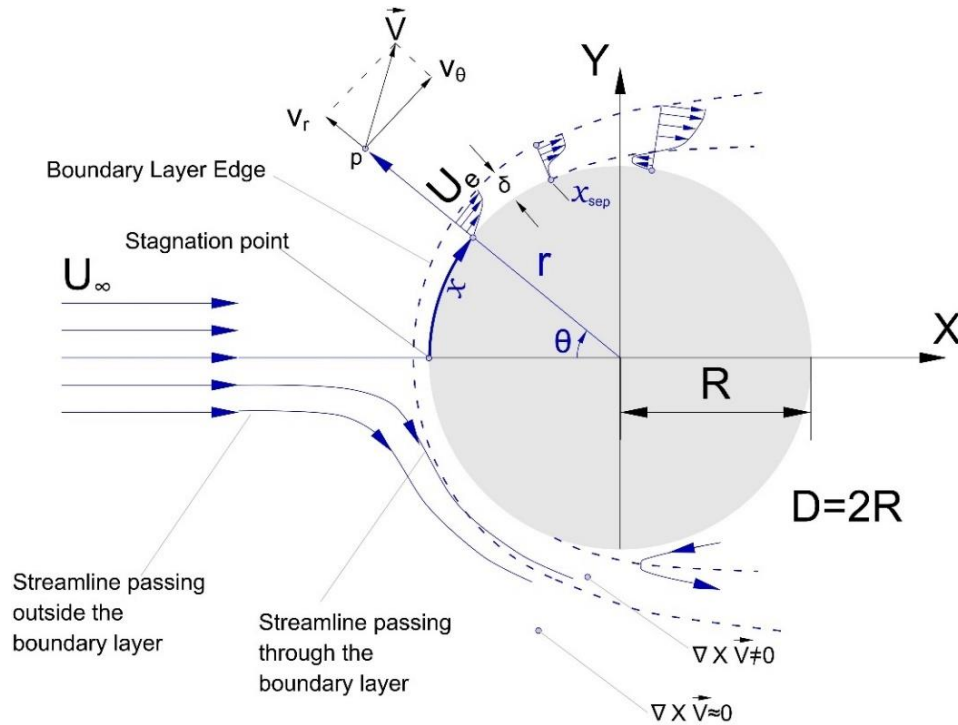


Figure 2: Schematic of viscous flow over a circular cylinder.

As the flow approaches the stagnation point the velocity reaches zero and the static pressure reaches its maximum. Along the surface of the circular cylinder the flow reaccelerates causing drop in the static pressure. Under restricted assumptions, Bernoulli's principle can be utilized to connect the drop in pressure with the edge velocity distribution. More details on the assumption will be discussed in this section. Before viscous effects are analyzed, inviscid analysis is considered for the first part of the discussion.

A quick estimate of surface pressure distribution for inviscid attached flow over a circular cylinder can be done by using the superposition of potentials for uniform velocity and doublet flow from linear potential flow theory [8,9]. If the inviscid flow regime is considered as irrotational, $\nabla \times \vec{V} = 0$, then the velocity can be expressed in terms of a scalar potential, $\phi(r, \theta)$, in polar coordinate as follows:

$$\vec{V} = \nabla \phi \quad \vec{V} = v_r \hat{r} + v_\theta \hat{\theta} \quad (1)$$

$$v_r = \frac{\partial \phi}{\partial r} \quad v_\theta = \frac{1}{r} \frac{\partial \phi}{\partial \theta} \quad (2)$$

Note that in a standard polar coordinate system, the angle measured in the anticlockwise direction is taken as +ve. However, in this document θ is measured in clockwise direction is taken to be +ve. The continuity equation for steady incompressible flow is $\nabla \cdot \vec{V} = 0$ which reduces to a linear Laplace equation in ϕ for irrotational flows (i.e. $\nabla \times \vec{V} = 0$):

$$\nabla^2 \phi = 0 \quad (3)$$

The inviscid attached flow over a circular cylinder can be modelled using superposition of potential for uniform flow, $\phi_{Uniform}$, and a doublet flow, $\phi_{Doublet}$ as shown in Fig. 3.

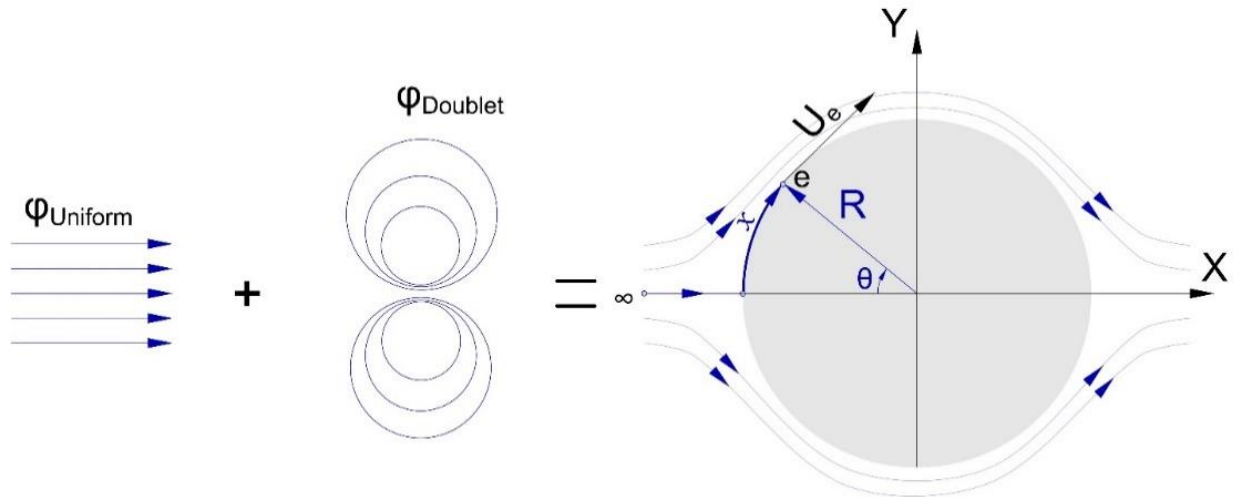


Figure 3: Potential flow model for circular cylinder.

The details of derivation for inviscid potential flow analysis for a cylinder can be found in literature [8,9]. Note that in literature $+\theta$ is taken in anticlockwise direction, however in this document $+\theta$

is taken in clockwise direction. The derivation yields [8] flow field velocity distribution for a circular cylinder with radius R in polar co-ordinates ($+\theta$: clockwise) as follows:

$$v_\theta = U_\infty \sin \theta \left(1 + \frac{R^2}{r^2} \right) \quad v_r = -U_\infty \cos \theta \left(1 - \frac{R^2}{r^2} \right) \quad (4)$$

Since the viscous effects are neglected in potential flow analysis, the edge conditions at point, e, in Fig. 3 is same as the conditions on the cylinder surface. To obtain edge velocity distribution on the cylinder surface for the inviscid case, the radial coordinate is set at $r = R$ in the above equations which yields:

$$U_e = v_\theta \text{ at } r=R = 2U_\infty \sin \theta \quad v_r \text{ at } r=R = 0 \quad (5)$$

Here U_e is taken as the tangential velocity, i.e., v_θ component, along the surface of the cylinder. Note that for viscous case (refer Fig. 2), the edge conditions refer to $r = R + \delta$.

Outside the viscous dominated region, i.e., beyond the edge of the boundary layer, the flow can be considered irrotational ($\nabla \times \vec{V} \approx 0$) and incompressible in the case Mach numbers, $M_\infty = U_\infty/a_\infty$, less than 0.3. For such inviscid, incompressible, irrotational steady flow, Bernoulli principle can be utilized for estimating the static pressure on a streamline that passes through point e from ∞ :

$$p_e + \frac{1}{2} \rho_\infty U_e^2 = p_\infty + \frac{1}{2} \rho_\infty U_\infty^2 \quad (6)$$

Rearranging:

$$p_e = p_\infty + \frac{1}{2} \rho_\infty U_\infty^2 - 2\rho_\infty U_\infty^2 \sin^2 \theta \quad (7)$$

Note that, just like the edge velocity U_e , the static pressure p_e is also a function of θ (or x). Often, it is convenient to represent the pressure distribution in terms of a non-dimensional form, i.e. coefficient of pressure:

$$C_p \equiv \frac{p_e - p_\infty}{\frac{1}{2} \rho_\infty U_\infty^2} \quad (8)$$

Substituting equation (7) in equation (8):

$$C_p = 1 - 4 \sin^2 \theta \quad (9)$$

In Fig. 4, the ideal surface pressure distribution from equation (9), is compared with typical measured pressure at subcritical and supercritical regimes.

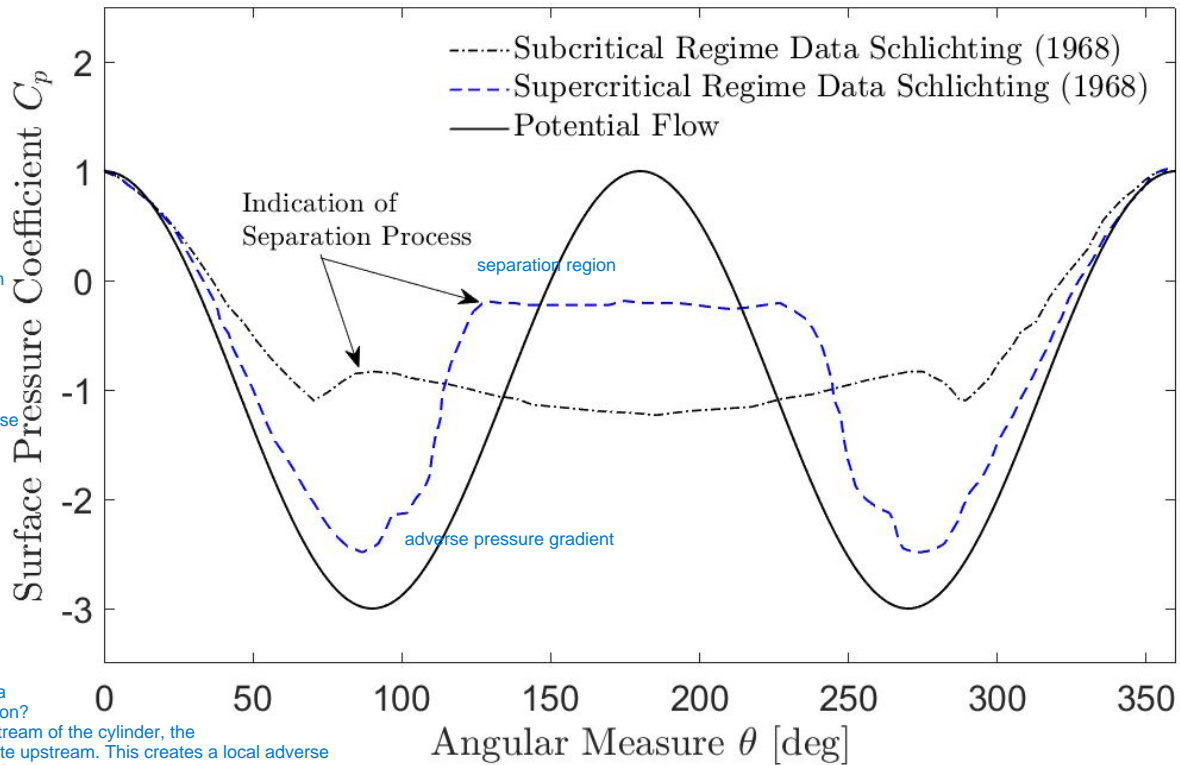


Figure 4: Static pressure coefficient along the surface of a circular cylinder.

For flow regimes with boundary layer separation, the pressure distribution is completely different from the ideal scenario. However, the pressure profile distribution estimated from equation (9) can be applied for creeping flow regime i.e., $Re_D < 4$. An important observation is that the separated flow phenomena which appears downstream along the cylinder surface strongly influences the upstream pressure profile and vice-versa. Therefore, there is a strong coupling between inviscid and viscous phenomena which cannot be decoupled for flow over bluff bodies like cylinders. As a result, a credible way to study such problems requires detailed experiments and/or detailed numerical solutions to Navier-Stokes equations using computational fluid dynamics tools.

Although the inviscid analysis provides an estimated range of pressure and velocity over in the forebody region of the circular cylinder, the viscous phenomena has a strong influence on the flow characters. When analyzing real flow, the edge conditions (i.e. at desired point e) are considered at $r = R + \delta$ as shown in Fig. 5. Note that a given any desired location of e , there exists a unique streamline that passes through it. The boundary layer is depicted by a dotted curve in Fig. 5 and it represents the loci of all the points where the condition $v_\theta \text{ at } (r=R+\delta) \approx 0.99 \times U_e$ is satisfied and must not be misinterpreted as a streamline.

A streamline that passes through point e is shown by a solid curve in Figure 5. Between the points ∞ and e , the streamline lies outside the boundary layer. Therefore, the total pressure-head remains constant between points ∞ and e using the Bernoulli's equation (Eq. 6). This can be leveraged to find the boundary layer edge velocity at point e .

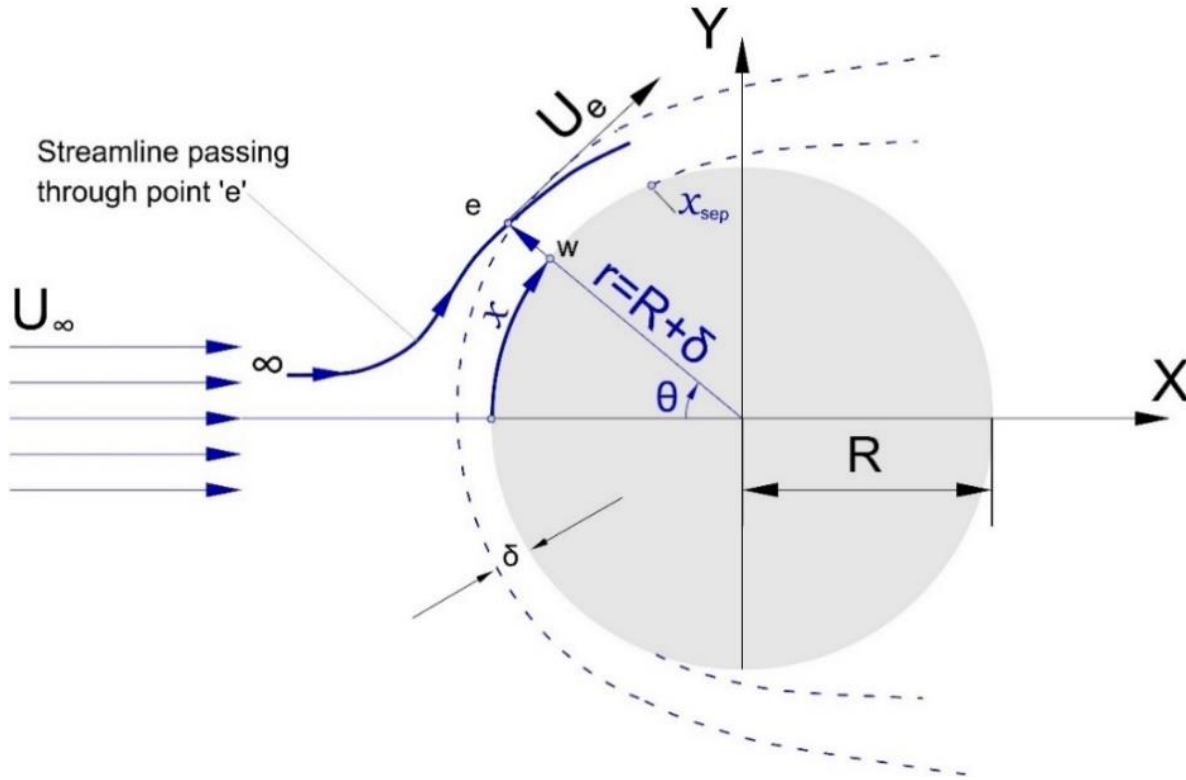


Figure 5: A streamline in viscous flow over a circular cylinder.

If the static wall pressure p_w is measured along the surface of the cylinder, then the corresponding boundary layer edge velocity can be obtained by applying Bernoulli equation along a streamline as shown in Fig. 5 with the assumption that the wall pressure (at point w) is same as boundary layer edge pressure at point e (i.e. $p_e \approx p_w$):

$$U_e = \sqrt{\frac{2}{\rho_\infty}(p_{o,\infty} - p_w)} \quad p_{o,\infty} = p_\infty + \frac{1}{2}\rho_\infty U_\infty^2 \quad (10)$$

While the above equation can provide an estimate of edge velocity using measurements of wall pressure, p_w , it is important to understand the assumptions and limitations of this equation. To begin with, the equation (10) can be applied only along an attached streamline. Therefore, estimates of velocity cannot be made after the separation point. Therefore, only between $x = 0$ to $x = x_{sep}$ we can obtain the edge velocity distribution of the flow.

Since there is a boundary layer thickness, δ , between the wall and the edge of the boundary layer, it is important to ensure that there is no strong pressure gradient normal to the wall (i.e. along r) which can cause significant difference between the wall pressure, p_w , that is measured and the static pressure at the boundary layer edge, p_e . To investigate this, consider the following order-of-magnitude analysis with radial pressure gradient causing centripetal acceleration (i.e. radial momentum equation):

$$\frac{\partial p}{\partial r} \approx \frac{\rho_{\infty} v_{\theta}^2}{R} \quad (11)$$

If the fluid element with thickness of the boundary layer is considered, $\Delta r \sim \delta$, and the average velocity of the fluid element inside the boundary layer is $v_{\theta} \sim U_e/2$, then using the above equation order-of-magnitude analysis yields the difference in pressure $\Delta p = (p_e - p_w)$:

$$\frac{\Delta p}{\Delta r} = \frac{\Delta p}{\delta} \sim \frac{\rho_{\infty} \left(\frac{U_e}{2}\right)^2}{R} \quad (12)$$

If the boundary layer is thin in the attached region (which is typical in the case of Laminar flow), then $\delta \ll R$. Rearranging the above equation, we get:

$$\frac{\Delta p}{\frac{1}{2} \rho_{\infty} U_e^2} \sim \frac{\delta}{2R} \ll 1 \quad (13)$$

very small quantity.
cylinder diameter

Therefore, Δp , is much smaller than the order of local edge dynamic pressure, $1/2 \rho_{\infty} U_e^2$. Consequently, the wall pressure is almost same as the boundary layer edge static pressure $p_w \approx p_e$. This enables to estimate the edge velocity of the flow using wall pressure measurement in equation between $x = 0$ and $x = x_{sep}$. Therefore, if the boundary layer thickness is large compared to R then the assumption that $p_w = p_e$ becomes invalid.

B. Drag Force on a Cylinder

In general, the net drag force arises from both pressure and shear distribution along the surface of the cylinder. When the flow separates, a strong asymmetry in pressure distribution is introduced between the fore and the aft part of the cylinder. This causes the pressure drag to account for about more than 90% of the total drag on the cylinder. The remaining portion is due to skin-friction drag from the viscous shear. In the case of creeping flow regime, $Re_D < 4$, the opposite is true i.e., a major portion of the drag originates from viscous shear when compared to pressure distribution. For the scope of this lab work, emphasis will be laid on pressure drag.

Consider the Fig. 6 which details the aerodynamic forces acting on the cylinder due to a free stream oriented along X-axis. The drag force (along X-axis) from pressure on an element with arc length $Rd\theta$ and span length L is given by (+ θ : clockwise):

$$dF_D = p_w \cdot \cos \theta \cdot L \cdot Rd\theta \quad (14)$$

Integrating from $\theta = 0, 2\pi$, yields total pressure drag on a cylinder with radius R (or diameter $D = 2R$) and length L :

$$F_D = \int_0^{2\pi} p_w \cdot \cos \theta \cdot L \cdot Rd\theta \quad (15)$$

CFD Drag >>>

Often the drag is expressed in terms of non-dimensional form as coefficient of drag, C_D which is given by:

$$C_D = \frac{F_D}{\frac{1}{2} \rho_\infty U_\infty^2 A_{ref}} \quad (16)$$

The reference area here is taken as the frontal area of the cylinder, $A_{ref} = L \cdot D$.

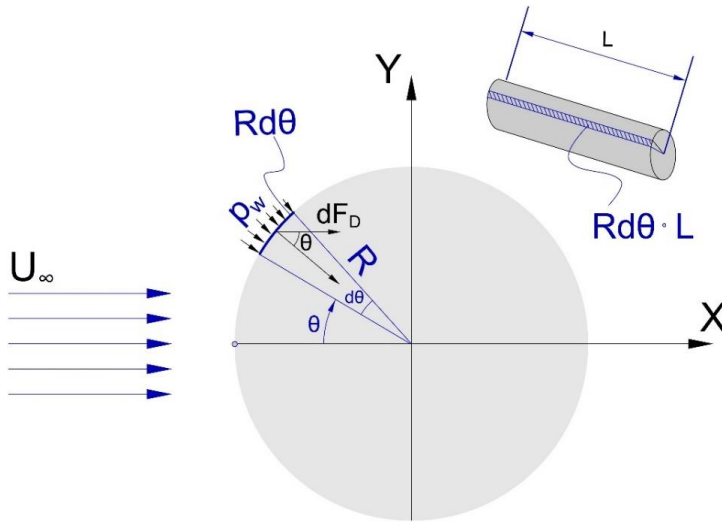


Figure 6: Elemental drag force on a circular cylinder.

Non-dimensional analysis using Buckingham Pi theorem [9] indicates that the drag coefficient is function of $C_D(Re_D, M)$. At low Mach numbers ($M < 0.3$) in the incompressible regime the coefficient of drag only depends on the Reynolds number only $C_D(Re_D)$. Experimental data on $C_D(Re_D)$ is widely available and typical variation of C_D with Reynolds number is shown in Fig 7.

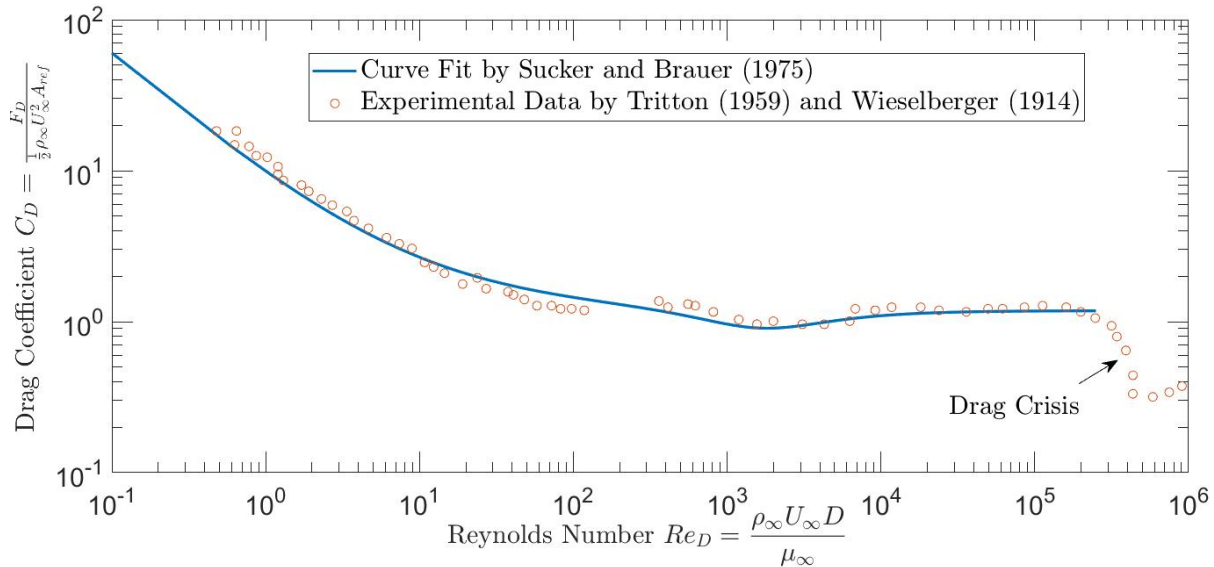


Figure 7: Drag coefficient of a circular cylinder with Reynolds number.

The variation of coefficient of drag with Reynolds number is characterized by two constant values as shown in Fig. 7. The coefficient of drag, $C_D \approx 1.2$ at the end of the sub-critical regime

and $C_D \approx 0.3$ at the start of the supercritical regime. The coefficient of drag in the critical regime is significantly influenced from boundary layer transition to external parameters, such as the cylinder roughness, the free-stream turbulence intensity, the blockage ratio D/H of the wind-tunnel with test-section height H . In subcritical regime, the forebody boundary layer is laminar and in critical regime the forebody boundary layer is turbulent.

It is important to note that the decrease of values of C_D with increase in U_∞ (or Re_D) should not be interpreted as decrease in the drag force. In fact, the drag force increases with U_∞ (or Re_D) as F_D is obtained as the product of C_D , A_{ref} and dynamic pressure $1/2 \rho_\infty U_\infty^2$. An accurate curve-fit was provided by Sucker and Brauer [10] which is valid only for subcritical regime $10^{-4} < Re_D < 250,000$. Such curve-fits must be used only inside within its specified validity range.

$$C_{D \text{ fit}} \approx 1.18 + \frac{6.8}{Re_D^{0.89}} + \frac{1.96}{Re_D^{1/2}} - \frac{0.0004 Re_D}{1 + (3.64 \times 10^{-7}) Re_D^2} \quad (17)$$

During experiments in the wind tunnel, it must be noted that the walls of the wind tunnel influence the streamlines passing over a bluff body. This is visualized in a schematic in Fig. 8. Therefore, the drag force will be different for flow over a cylinder with and without the blockage effects from the wind tunnel walls (or confinement). For this Allen and Vincenti [11], provided an equation to correct for the wind tunnel blockage effect using image doublets to represent the interference between the wall and the cylinder. The corrected C_{Dc} which “removes” the influence of wall confinement from the measured drag coefficient C_D for a circular cylinder in a wind tunnel:

$$\frac{C_{Dc}}{C_D} = 1 - \frac{1}{2} C_D \left(\frac{D}{H} \right) - 2.5 \left(\frac{D}{H} \right)^2 \quad (18)$$

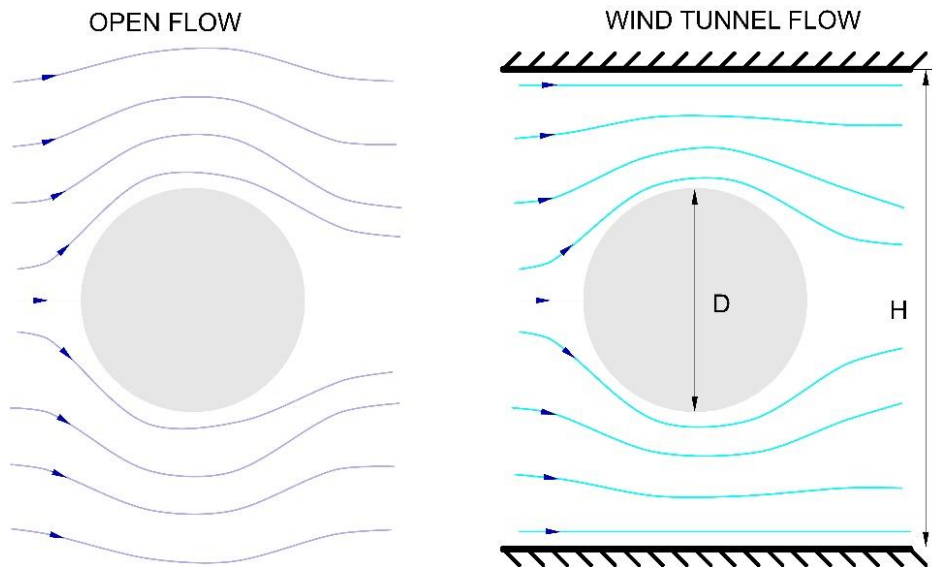


Figure 8: Schematic comparing the streamlines pattern between open and confined wind tunnel flow over a circular cylinder.

Note that wind tunnel blockage will also influence viscous phenomena like boundary layer growth and separation.

C. Boundary Layer Separation

To analyze the boundary layer separation let us consider $r - x$ coordinate instead of $r - \theta$ coordinate. Here x is simply the arc length measured from the forebody stagnation point. In this lab work since there is circular symmetry in the geometry, the arc length is given by $x = r \cdot \theta$ where θ must be expressed in radians. Note that X represents axis along the freestream in cartesian co-ordinate system, x represents arc-length in curvilinear coordinate system. The details of the coordinate system are described in the Fig. 5.

If the flow is rapidly slowed down through an adverse pressure gradient along the body ($dp/dx > 0$), then it is possible that the flow inside the boundary may not possess sufficient momentum to overcome the imposed adverse pressure gradient from the outer flow. The velocity profile becomes more like S-shaped while the wall shear starts to reduce. If the adverse pressure gradient is strong enough, the wall shear stress, τ_w , reaches zero at the wall with an existence of an inflexion point in the boundary layer velocity profile as shown in Fig. 2. At the point where τ_w or $\partial u/\partial y = 0$, the flow separates. Beyond which a separated region is formed and the flow reverses in its direction. The criterion for detecting separation is $\partial u/\partial y = 0$ or at the point where skin friction coefficient is zero. Alternatively, wall pressure profile can be used to approximately detect the flow separation region. In Fig. 4, the wall pressure abruptly begins to remain constant. This is also an approximate indication of separation point. It should be noted that not all boundary layers separate when they encounter an adverse pressure gradient. The separation can never occur for regions with favorable pressure gradient $dp/dx \leq 0$.

A turbulent boundary layer can draw more energy from the outer flow therefore it contains relatively fast-moving fluid parcels near the wall. While a laminar boundary layer contains slower moving fluid parcels near the wall. This means that, for the same value of the edge velocity, a

turbulent boundary layer would remain attached longer than a laminar boundary layer. The experimental data on the angular location of the separation point for different Reynolds number is plotted in Fig. 9.

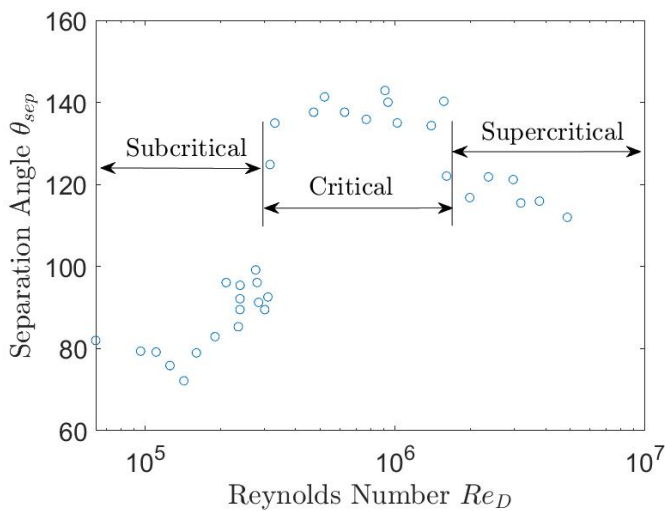


Figure 9: Experimental data on flow separation by Achenbach (1968) (refer [8]).

From the data it is observed that the laminar boundary layer separates prematurely in the subcritical regime when compared to the turbulent boundary layer in the supercritical regime. For the scope of the current lab work, emphasis will be laid on laminar separation in subcritical flow over a cylinder.

For subcritical conditions, the separation angle is close to $\theta_{sep} \sim 80^\circ$ which indicates that the separation point is located in the forebody region. This goes against basic intuition because the inviscid ideal pressure profile from potential flow solution indicates that until $\theta = 90^\circ$ there is favorable pressure gradient, $dp/dx < 0$ (see Fig. 4) and therefore separation cannot take place. However, in an actual flow there is a strong coupling between the wake flow and the upstream flow such that separated wake flow in the aft region modifies the upstream flow in the forebody region. As a result, the boundary layer edge velocity, $U_e(x)$, and pressure profile $p_e(x)$ distribution is significantly altered due to the separation process. This strong coupling process results in a velocity profile such that the forebody region contains regions with $dU_e/dx < 0$ (or $dp/dx > 0$). Therefore, the laminar separation occurs in the forebody region in the subcritical regime.

The inviscid ideal prediction of velocity profile was detailed in equation (5) which can be re-casted and represented in $r - x$ coordinate using Taylor series expansion of sin function:

$$\frac{U_e(x)}{U_\infty} = 2 \sin\left(\frac{x}{R}\right) = 2.0 \cdot \left(\frac{x}{R}\right) - 0.333 \cdot \left(\frac{x}{R}\right)^3 + 0.0167 \cdot \left(\frac{x}{R}\right)^5 \dots \quad (19)$$

The experimental fit data produced by Hiemenz flow at $Re_D \sim 10^4$ for edge velocity distribution in the forebody $U_e(x)$ is substantially altered by the wake flow and it is given by:

$$\left. \frac{U_e(x)}{U_\infty} \right|_{Hiemenz} = 1.814 \cdot \left(\frac{x}{R}\right) - 0.271 \cdot \left(\frac{x}{R}\right)^3 - 0.0471 \cdot \left(\frac{x}{R}\right)^5 \quad (20)$$

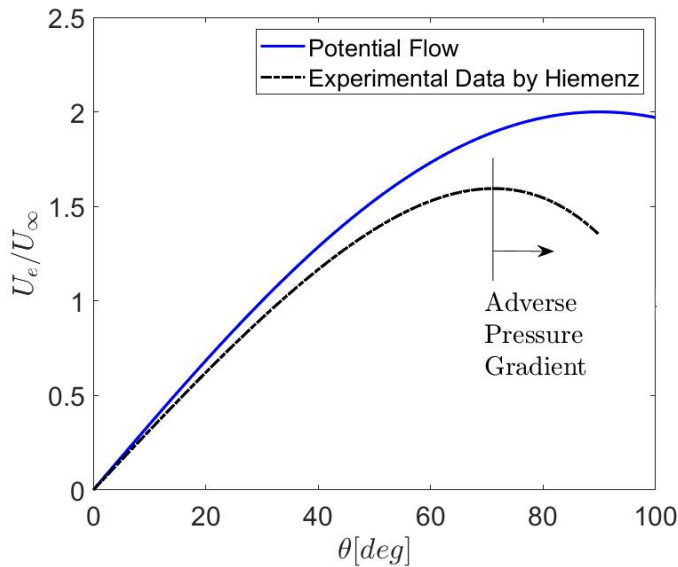


Figure 10: Edge velocity distribution for ideal and real flows.

Note that shape of the pressure profile in the subcritical range doesn't change much with Re_D . Therefore, the edge velocity profile in equation (20) obtained at $Re_D \sim 10^4$ has a wider applicability but limited to the subcritical regime. Equation 19 (ideal flow) and equation (20) (Hiemenz data) are plotted and compared in the Fig. 10.

It can be seen that the inviscid ideal and the real edge velocity profile in the forebody region is substantially different due to

the wake flow influence on upstream flow. The location of separation point determines the size of the wake region depend on the character of the forebody boundary layer and vice versa.

For any given arbitrary $U_e(x)$ profile on a bluff body, laminar boundary layer separation point can be predicted using integral boundary layer analysis. Particularly, Thwaites-Walz method is introduced here to analytically predict the separation point. For further reading on boundary layer equations, integral boundary layer methods and derivation of Thwaites-Walz method please refer to [6]. These methods can not only be used to predict separation but also for predicting the boundary thickness growth along the body. For the scope of this lab work only the procedure to implement Thwaites-Walz method to find the boundary layer separation point for a given $U_e(x)$ velocity is described here.

A non-dimensional momentum thickness, Λ , introduced in Thwaites-Walz method that is used to determine separation point. At a given arbitrary angular position, θ , on the circular cylinder the arc-length measured from $\theta = 0$ or stagnation point is $x = R \cdot \theta$ and the local value of $\Lambda(x)$ at this point is given by:

$$\Lambda(x) = \frac{0.45}{U_e(x)^6} \left(\int_0^x U_e^5(x) \cdot dx \right) \cdot \left(\frac{dU_e(x)}{dx} \right) \quad (21)$$

For different given position values of x on the surface of cylinder, the corresponding values of $\Lambda(x)$ is computed using equation. (21) The x –position at which $\Lambda(x_{sep}) \approx -0.09$ indicates the location of the separation point. Once the x_{sep} is obtained, the corresponding angular position can be retrieved using $\theta_{sep} = x_{sep}/R$. In this lab work, as part of the report requirements (as detailed in section VI), it is required to compute and predict the separation point using ideal inviscid profile (equation 19) and Hiemenz corrected profile (Eq. 20) for the designed cylinder. These predicted values must then be compared with experimentally obtained separation point position from the pressure profile data and computationally using CFD from c_f data. Potential discrepancy between experiments and theory may arise due to early transitions in the flow caused by free-stream turbulence, surface roughness, wind-tunnel confinement, finite span effects etc.

The flow over cylinder or any bluff body with a large-separated region is a cautionary tale for using reduced order boundary layer analysis. In such type of reduced analysis, first the inviscid flow is solved using potential flow analysis to obtain $U_e(x)$. Then this profile is imposed as an input to the reduced viscous flow equations to predict the flow parameters inside the boundary layer. Often the displacement thickness obtained from the first iteration of boundary layer solution is added to the solid body to recompute the potential flow solution and its corresponding viscous solution for an improved accuracy. Such decoupled iterative analysis between inviscid and viscous flows can be used for thin aerodynamic objects where the coupling between the inviscid potential flow and the viscous phenomena is weak. For flow over a cylinder with large-separated region that contains a strong coupling between viscous and inviscid phenomena, reduced order decoupled iterative analysis cannot be used directly to obtain accurate solutions. Therefore, experiments and numerical solutions to Navier-Stokes equations are required.

V. Experimental Setup

The experiment for flow over cylinder is carried out in a low-speed subsonic wind tunnel, AF100, as shown in Fig. 11. The AF100 wind tunnel is open return suction type having a closed test section. It is supported by a steel tubular structure for improved mobility/easiness of installation.

Air enters the tunnel through a bell-mouth diffuser that accelerates the flow through a honeycomb flow straightener which has the main purpose of **reducing the lateral velocity components coming from the swirling motion of the air in the room**. The air stream enters the test section and exits by passing through a protective grid before moving through the variable speed axial fan. Downstream the axial fan is located a silencer. The speed of the axial fan and, thus, the nominal velocity in the test section is controlled by an electric drive control in the Control and Instrumentation Unit (white front panel in Fig. 11).



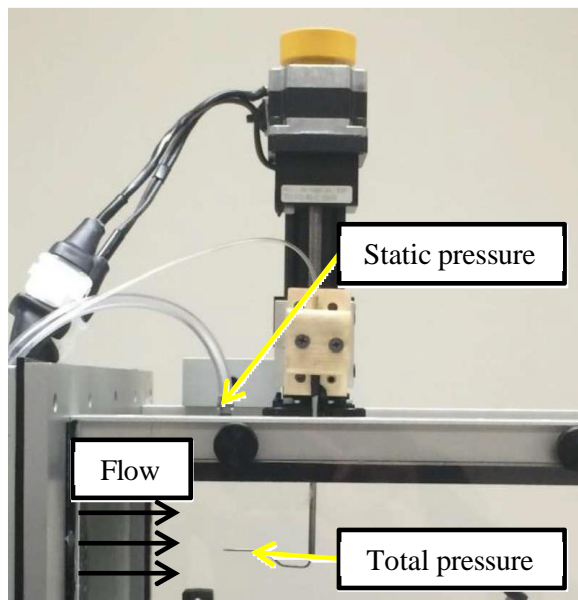
Figure 11 AF100 low speed subsonic wind tunnel.

The test section has a square cross section with cross section, **12" × 12"**, which is enclosed with acrylic transparent panels. Each lateral panel is equipped with supports for the various models and force balance available. **Four holes are located on the top panel of the test section to locate the two Pitot devices and the two static-pressure ports upstream and downstream the center of the working section.**

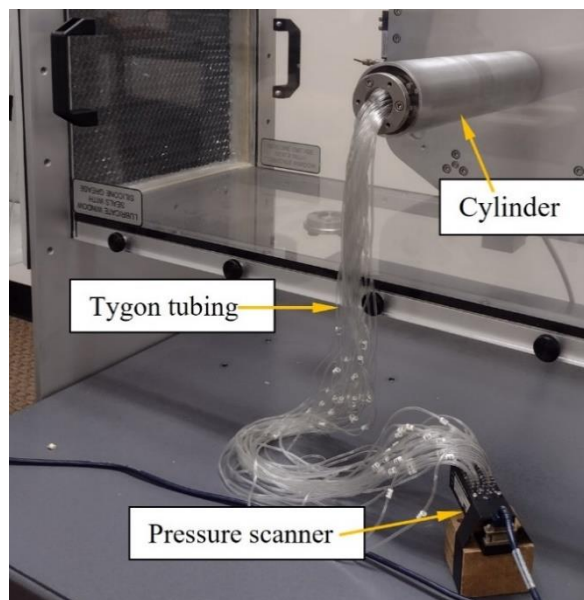
Specifically for this experiment, a Pitot tube is mounted on the slide which has a vertical travel of 4 cm to span part of the tunnel core (Fig. 12(a)) and, thus, to measure the average free stream velocity using:

$$V_{\infty} = \sqrt{\frac{2(P_{pitot} - P_{static})}{\rho_{\infty}}} \quad (22)$$

For this experiment, only the analog manometer connected to the AF100 control board is used to measure the differential pressure, $(P_{pitot} - P_{static})$.



(a)



(b)

Figure 12 (a) Pitot and static pressure ports (b) Wind tunnel setup for flow over cylinder.

A 32-channels pressure scanner (Fig.12(b)) is used, in addition to the analog manometers, in order to collect the surface pressure on selected ports on the cylinder. The data stream from the pressure scanner are collected by the DTCNetX software from the Ethernet port and converted directly to psig. Among the 32 available channels, 30 of them are used for flow over cylinder experiment.

The ESP-32HD is a miniature differential pressure scanner module that allows for multiple measurements of dry, non-corrosive gases to be taken. The scanner integrates 32 silicon piezoresistive pressure sensors ranging from ± 1 psid. Each pressure sensor incorporates a temperature sensor and EEPROM for storage of calibration data as well as sensor identification information such as pressure range, factory calibration date, and user-managed last or next calibration date. The microprocessor uses the data from the EEPROM to correct for sensor zero, span, linearity and thermal errors. The scanner also provides digital temperature compensation capability of the sensors to reduce thermal errors. Proper and periodic on-line calibration maintains system accuracy of up to $\pm 0.03\%$ FS (Full Scale) after re-zero. The output of the sensors is electronically multiplexed through a single onboard instrumentation amplifier at rates up to 50,000 Hz using binary addressing. This binary pressure data is then relayed through an auto-negotiating 10 or 100 Mbit Ethernet interface. The binary pressure data is scaled to engineering units of psig (differential) within the host DCTNetX interface software and written into a storage Excel data file on the PC. The cylinder construction is shown in the Fig. 13

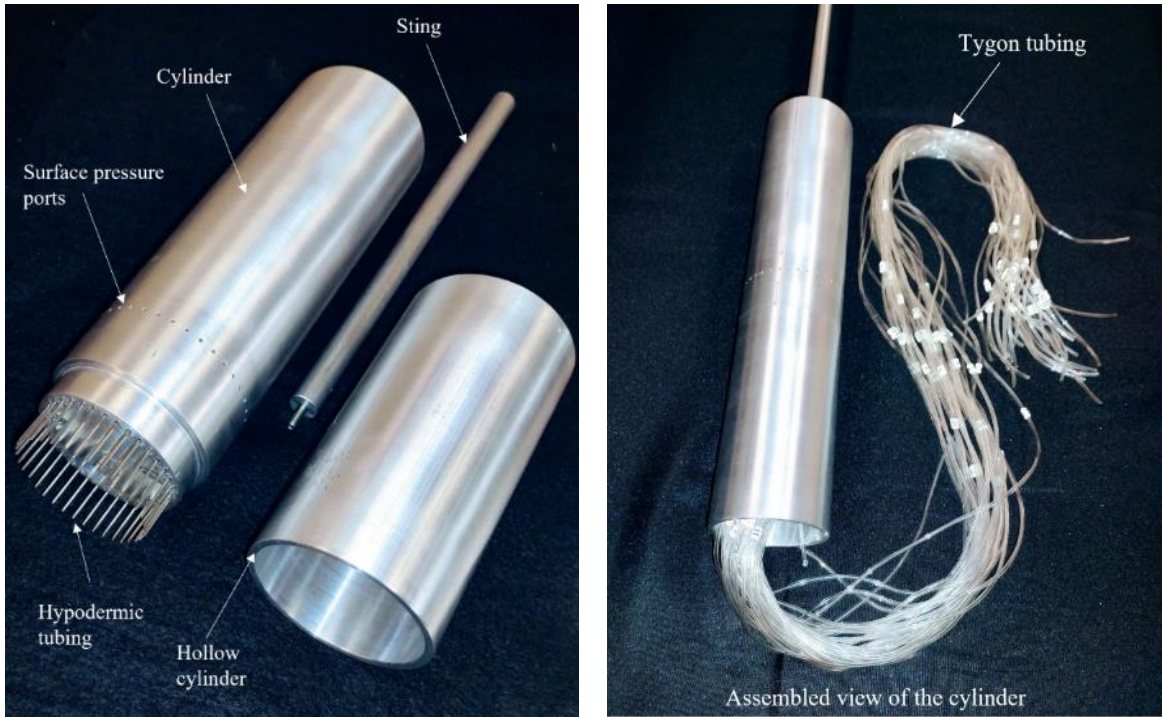


Figure 13 Cylinder construction and its parts.

The cylinder has 36 holes that act as pressure ports. These holes are placed at 10[deg] apart from each other as shown in Fig. 14. For the experiment only 30 ports are used. Since the pressure scanner has only 32 ports available and retaining two ports as service ports it was decided that 30 channels for static pressure on the cylinder to be used. Since the pressure in the base region of the cylinder remains constant due to separation, a smaller number of pressure ports are used in the separated region. The port diagram used for this experiment is detailed in Fig. 14 along with a table containing the port positions.

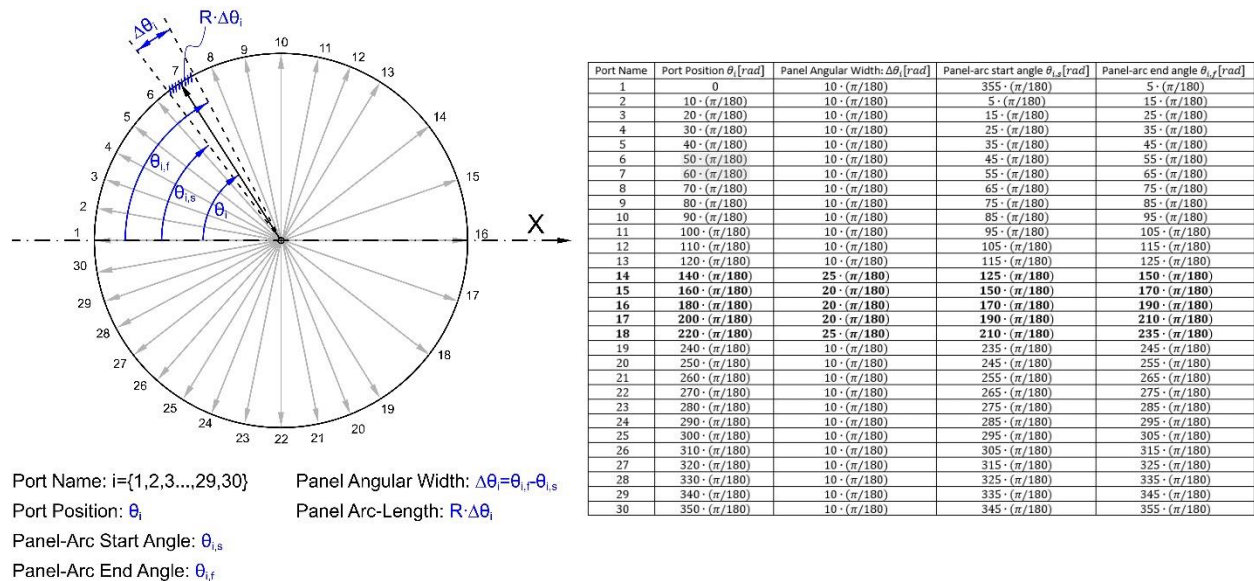


Figure 14 Port nomenclature and panel dimensions.

For this experiment, the circle is divided into 30 panels as shown in Fig. 14. Each panel is associated with a port. It is assumed that in the neighborhood of a given port, the static pressure across the corresponding panel is constant. For example, consider the pressure port-7 sketched in Fig. 14 that is located at $\theta_i = 70[deg]$. The corresponding panel-arc for port-7 spans from $\theta_{7,s} = 65[deg]$ to $\theta_{7,f} = 75[deg]$. The static pressure is assumed to be constant over the panel-arc spanning from $\theta_{7,s}$ to $\theta_{7,f}$, and equal to the time-averaged pressure recorded on port 7 (i.e. p_7). Note that during the integration process to find the drag coefficient, the term θ which appears in equation (15) is expressed in radians. Therefore, the port position and its corresponding panel width is given in radians in the table (see Fig. 14). The integral then reduces to a discrete summation as follows:

$$F_{D,exp} = \int_0^{2\pi} p_w \cdot \cos \theta \cdot L \cdot R d\theta \approx \sum_{i=1}^{30} \left(\int_{\theta_{i,s}}^{\theta_{i,f}} p_w \cdot \cos \theta \cdot L \cdot R d\theta \right) \quad (23)$$

Pw, L and R constant

Evaluating the integral, we get

$$F_{D,exp} \approx \sum_{i=1}^{30} p_i \cdot L \cdot R \cdot (\sin(\theta_{i,f}) - \sin(\theta_{i,s})) \quad (24)$$

Recall the definition of drag coefficient in equation (16). The drag coefficient corresponding to experimental data is obtained by using

$$C_{D,exp} = \frac{F_{D,exp}}{\frac{1}{2} \rho_{\infty} U_{\infty}^2 A_{ref}} \quad (26)$$

Recall $A_{ref} = L \cdot 2R$. Relevant dimensions of the cylinder assembly are the diameter, D , and axial length, L that are given by:

$$D = 2.5'' \quad \& \quad L = 11.8''$$

A. Experimental Procedure

Using the instructions below, the Pitot tube will be used to measure the dynamic pressure and, thus, to calculate the freestream velocity. The wind tunnel motor contains a drive unit which changes the input electrical power accordingly to the position of the speed knob on the control panel. Below are listed all the steps to be performed in order to complete the experimental campaign in the subsonic wind tunnel:

1. Record the room temperature and the atmospheric pressure (P_{tot}) by using the thermometer and the barometer on the wall.
2. Open the DTCNetX pressure scanner interface and connect the DTCNet DAQ using the "TCP" connection under the "Comms." tab.
3. Set the name of the data file as "C:\Program Files \DTCNetX\pressure_data.csv" using the "Logging File" textbox under the "Setup" tab. Note, this will be the path and filename for data storage. In this case the .csv filename is "pressure_data".
4. Set the data acquisition parameters under the "Data Buffer" tab to the following:

- Stop the data collection "After a single cycle".
 - Set the number of cycles to $n = 1$
 - Ensure the "Log to Disk at Every Event" option is checked.
 - Start the data collection "On Demand".
 - Set the "Samples per Cycle" to 100.
5. Manually zero the pressure scanner to eliminate any potential offset by clicking the "0.000" tab.
 6. Align the cylinder such that the leading edge (first pressure tap) is at zero AoA to the incoming flow. This done by observing the ports on either side of first pressure taps i.e. port 2 and port 30. The alignment is done such that port 2 and port 30 reads the same value of pressure.
 7. Start the wind tunnel to the test speed and wait for the flow to become steady. You can see this by monitoring the analog manometer connected to the pitot tube and static port. Record the dynamic pressure from the analog manometer in *mm of H₂O*. This will be used to calculate the freestream velocity.
 8. Under the "Data Buffer" tab press the start button on the left-hand side of the DTCNetX panel. A red light indicator should appear in the first white box in the upper right of the panel. The data collection procedure should take approximately 3-5 seconds. After the data acquisition is complete a green light indicator should momentarily appear in place of the second white box before all three boxes return to the nominal white color. After recording the first set of measurements check and ensure the data is writing to the correct file under the specified path.

B. Data Reduction

The data from the spreadsheets created from the DTCNetX software must be reduced using the procedure outlined in this subsection.

1. Convert the unit of pressure data from the barometer attached to the wall (p_{room}), from mmHg to Pa by using the conversion factor, 1 mmHg=133.3224 Pa.
2. Calculate the density of the air by the ideal gas law from the room temperature and pressure measurements. ($\rho_{\infty} = p_{room}/(R \cdot T_{room})$)
3. Convert the unit of the pressure data from the analog manometers to Pa by using the conversion factor, 1mm H₂O = 9.8065 Pa.
4. Calculate the flow velocity using Bernoulli equation and the manometer reading for the dynamic pressure.
5. Calculate the local pressure coefficients by using both the Pitot probe reading, differential pressure from manometer and the pressure scanner reading. Recall the definition of the local pressure coefficient:

$$C_{p,i} = \frac{p_i - p_\infty}{\frac{1}{2} \rho_\infty V_\infty^2} \quad (27)$$

- 6. Use equation to obtain the time-averaged drag force and its corresponding drag coefficient.

V. Computational Fluid Dynamic Analysis Setup

Many fluid flow phenomena of practical importance can be analyzed using Navier-Stokes equations. These are set of non-linear partial differential equations which describe the application of Newton's second law of motion to fluid flow. In computational fluid dynamics (CFD), the Navier-Stokes equations along with mass continuity and energy conservation equations are discretized and numerically solved to get a physical insight about the flow field and to make quantitative predictions about the flow characteristics. In order to perform a numerical simulation, first a computational domain should be defined, which includes the geometry and the flow field of interest. The entire computational domain is then divided into different cells (triangular, tetrahedral, quadrilateral, hexahedral, etc.) through a process called meshing, also known as grid generation. The more the number of cells, the more will be the spatial resolution and higher the accuracy. For unsteady flows, the time step size determines the temporal resolution of the flow features. The discretized (spatially and temporally) Navier-Stokes equation is then solved at each of the cell intersection points (nodes) to obtain the final solution.

A 2D unsteady laminar Navier-Stokes solver available in ANSYS Fluent was used to simulate the flow past cylinder. The pertinent governing equations are the continuity and momentum (Navier-Stokes) equations in 2D as shown in Eq (28 – 30).

$$\frac{\partial u}{\partial x} + \frac{\partial v}{\partial y} = 0 \quad (28)$$

$$\frac{\partial u}{\partial t} + u \frac{\partial u}{\partial x} + v \frac{\partial u}{\partial y} = -\frac{\partial p}{\partial x} + \mu \left(\frac{\partial^2 u}{\partial x^2} + \frac{\partial^2 u}{\partial y^2} \right) \quad (29)$$

$$\frac{\partial v}{\partial t} + u \frac{\partial v}{\partial x} + v \frac{\partial v}{\partial y} = -\frac{\partial p}{\partial y} + \mu \left(\frac{\partial^2 v}{\partial x^2} + \frac{\partial^2 v}{\partial y^2} \right) \quad (30)$$

Note that the results obtained from this simulation is valid only near the cylinder. In the wake region away from the cylinder, the flow can undergo transition to turbulence and the usage of proper turbulence models is necessary to capture the wake region properly.

A. Computational Domain and Grid Generation

Computational domain is a region around the geometry (in this case, cylinder) where the solution for the governing equations is calculated. The geometric specification of the domain depends on the nature of the flow we are trying to solve. For example, in subsonic flows, the governing equations are elliptical in nature which allows any disturbance to propagate in all directions. So, the boundaries should be defined at large distance away from the geometry. The choice of a large computational domain will minimize the propagation of disturbance from the boundaries on the region near the geometry.

As mentioned in before, the diameter of the cylinder used here is 2.5in (0.063m). A square shaped computational domain is chosen for the present study. The dimensions of the computational domain are shown in Fig. 15. Please note that, all dimensions are normalized by dividing with the cylinder diameter. The horizontal and vertical extend of the domain is $64D$. The inlet and outlet planes of the computational domain are located at $24D$ and $40D$ respectively from the center of the cylinder. A larger extend of the domain is given aft of the cylinder to obtain a good visualization of the wake induced by flow over the cylinder. The entire computational domain is then discretized into number of smaller cells known as mesh or grids as shown in Fig. 16. The governing equations describing the flow are applied to these cells to simulate the local behavior of the flow. As the number of cells increases, the accuracy of the solution also increases. However, the computational resources required to perform a simulation increases with the number of cells. So, an optimum mesh distribution should be used which can guarantee reasonable accuracy at reasonable computational expense.

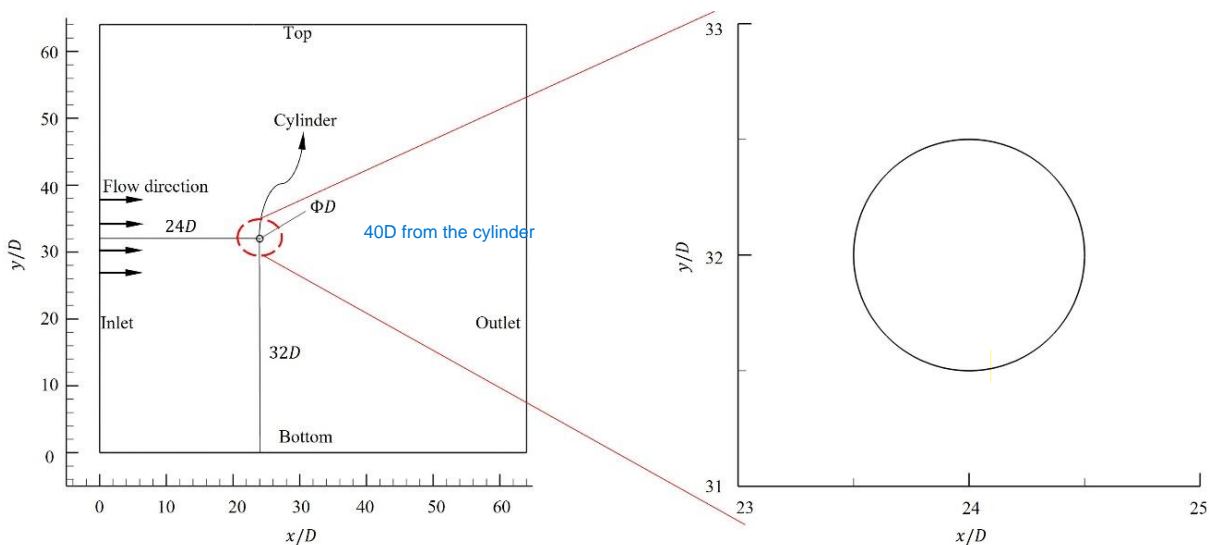


Figure 15 Computational domain

The computational domain shown in Fig. 16 was discretized using a combination of structured and unstructured grid. The unstructured grid with triangular and quadrilateral cells were

used in the region close to the cylinder whereas, structured grid was used in the region away from the cylinder. The total number of cells are approximately 87000. A denser grid distribution was used near the cylinder and in the wake region to better resolve the boundary layer and wake. The grid distribution at different regions in the flowfield is shown in Fig. 16. The first cell height near the cylinder wall is fixed as $3.4 \times 10^{-6} \text{m}$. In turbulent flow problems, the first cell height is fixed using y^+ criterion. But in laminar flows, there are no specific criterion to fix the first cell height. Since we are only interested in the flow phenomena close to the cylinder and the wake, a denser grid distribution is not necessary in regions away from the cylinder. Also, giving a denser grid distribution away from the cylinder will result in a higher number of cells in the computational domain and eventually lead to a significant increment in the computational cost. The transition between the higher and lower grid density regions should be smooth to reduce errors. In the current mesh, a monotonic rational quadratic spline (MRQS) distribution was used to establish a smooth gradient in the grid distribution.

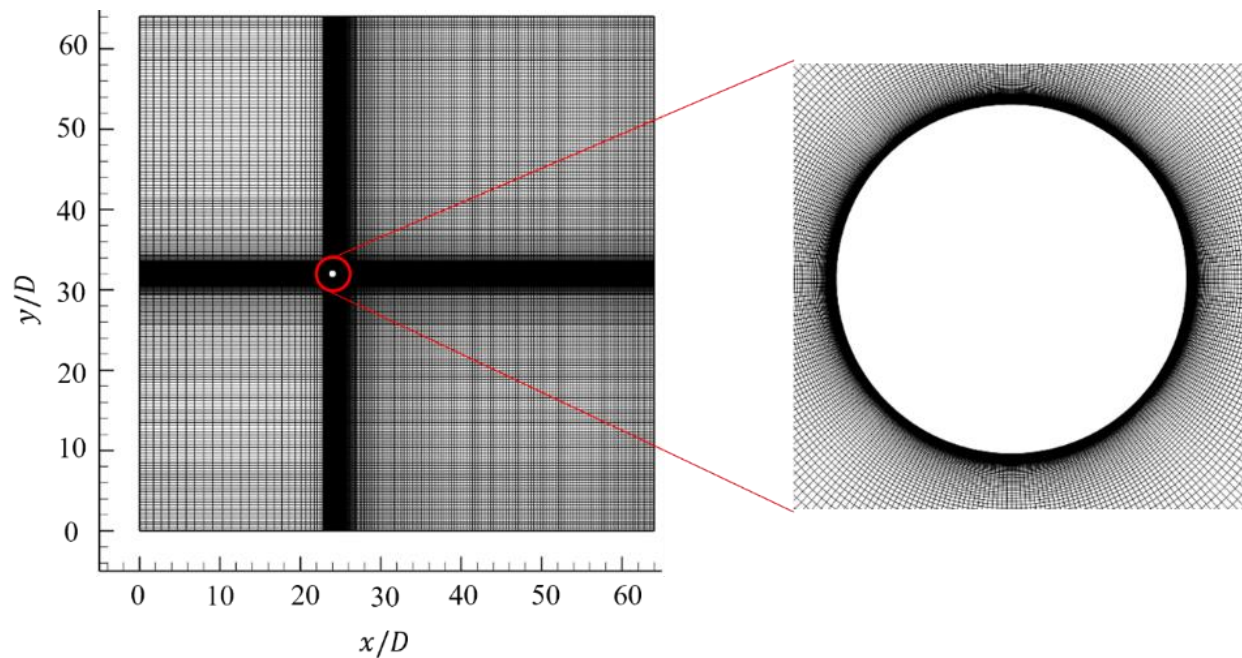


Figure 16 Mesh distribution

B. Boundary Conditions.

At the inlet boundary of the domain, a “velocity inlet” boundary condition was specified with a flow velocity of 25 m/s normal to the boundary. The top, bottom and the outlet boundaries of the domain are given an “outflow” boundary condition which ensures zero gradient for all flow variables in the direction normal to the boundary. This boundary condition is commonly used in incompressible flows when the pressure and velocity of the flow at the outlet are unknown. In this case, extrapolated values of the flow variables from the interior of the domain will be used at the outlet boundary. However, it should be noted that the “outflow” boundary condition is not suitable

for unsteady flows with variable density. Since there is no rotation for the cylinder geometry, the cylinder surface was treated as a “stationary wall” with a “no-slip” condition which ensures zero velocity at the wall.

C. Computational Procedure

The detailed procedure for performing the computational simulation is included as a video. The video file is uploaded along with the other case and data files on Canvas. Figure 18 shows the vortex shedding using contours of vorticity magnitude.

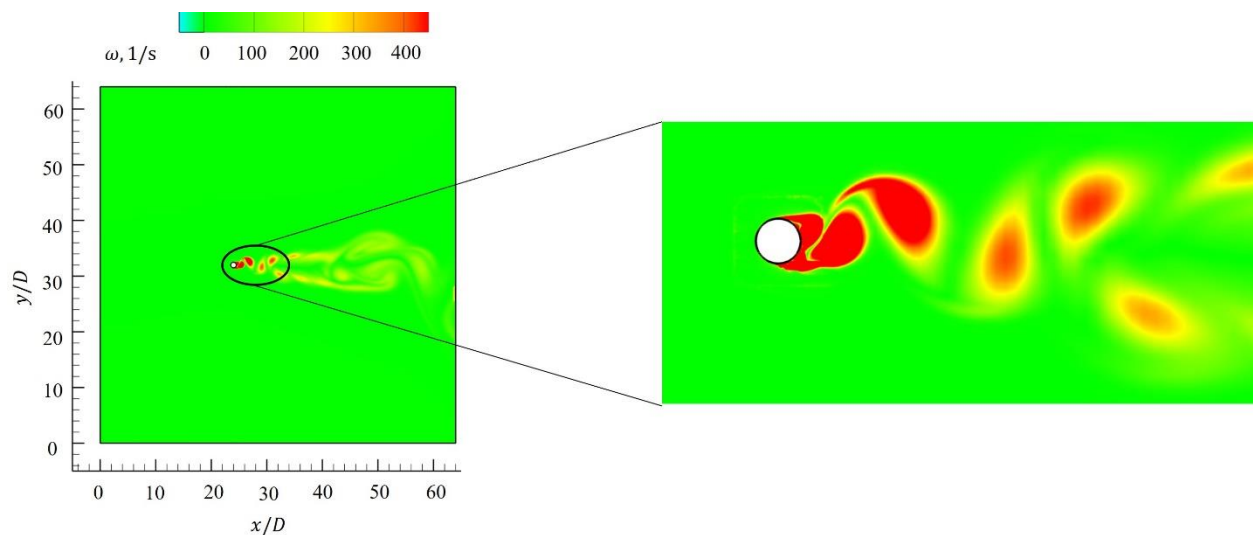


Figure 17 Vortex shedding shown using the contours of vorticity magnitude

D. Data Reduction

The details regarding setting up the computational simulation and extracting the data files are mentioned in an addendum video file named “**Flow over a cylinder_CFD**”. Once the data files are extracted, follow the below-mentioned steps to obtain the necessary results.

- 1. Open the file with wall static pressure data along the cylinder wall. The data file will contain the values of wall static pressure at different x-locations, starting from the leading edge. Remember that the x-coordinate of the cylinder leading edge is not at zero (See Fig. 15)
- 2. Copy the data into an EXCEL spreadsheet for post processing.
3. Convert the x-locations x_i to the corresponding azimuth angle θ_i using the schematic shown in Fig 18. Note that “ i ” is the index representing each data points.

- 4. Use the value of the freestream static pressure p_∞ as 133.63 Pa (The mean static pressure upstream of the cylinder)
- 5. Once p_∞ is known, determine the coefficient of pressure c_p . (Use Eq. 27)
- 6. Plot c_p vs θ_i
- 7. Open the file with wall shear stress data. The data file will contain the values of x-wall shear stress τ_{w_x} at different x-locations, starting from the leading edge.

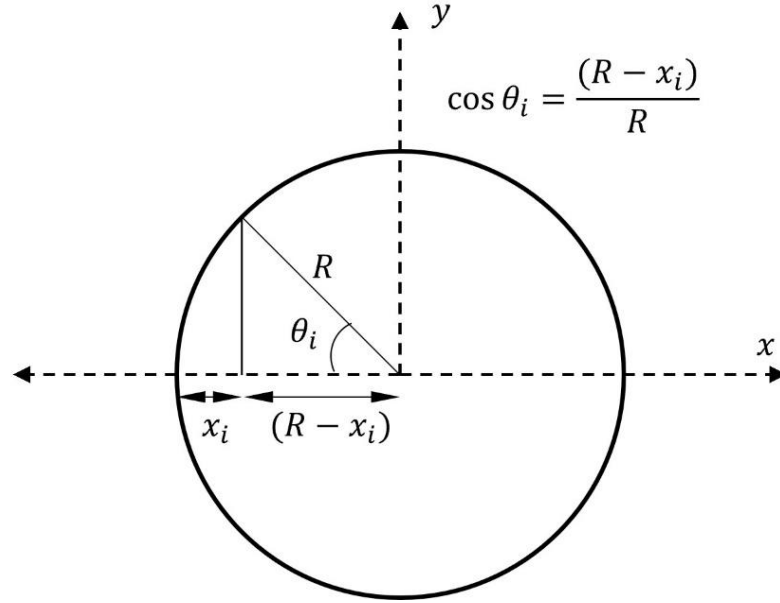


Figure 18 x_i to θ_i conversion

- 8. Calculate the skin friction coefficient c_f .

$$c_f = \frac{\tau_{w_x}}{\frac{1}{2} \rho_\infty U_\infty^2} \quad (31)$$

- 9. Follow step 3 to convert the x-locations x_i to the corresponding azimuth angle θ_i using the following schematic.
- 10. Plot τ_{w_x} vs θ_i

VI. Report Requirements How much theory?

Please Answer All the Requirements

- 1. Calculate the Reynolds number. (Use freestream velocity, density and pressure) Assumed Viscosity?
- 2. In which regime the flow is categorized as?
- 3. Plot coefficient of pressure v/s azimuth angle (Plot the results from inviscid, CFD and experiment in the same graph) Just check

- a. Determine the separation location. (Refer Fig. 4) For all?
4. Calculate the drag coefficient from the pressure tap measurements on **top and bottom surface** (**with** and **without** the wind tunnel correction). Show the calculations.
 - a. Obtain the drag coefficient from the experimental data. Check
 - b. Calculate the corrected drag coefficient using Eq. (18)
 - c. Calculate the pressure drag and the corresponding drag coefficient using the surface pressure distribution obtained from the CFD simulation
 - d. Compare the values of drag coefficients obtained in steps 4(a), 4(b) and 4(c) with the drag coefficient obtained from literature fit data in Eq. (17).
 - e. Comment on differences observed in the results obtained from four approaches.
5. Identify the separation point (θ_{sep} or x_{sep}/R) from experimental data, CFD data and analytical method.
 - a. Using experimental data of coefficient of pressure, determine the approximate separation point and reason your answer.
 - b. Using CFD data of wall shear stress obtain the separation point (Note: the value of wall shear stress will be almost zero for separation point)
 - c. Use Thwaites-Walz method for analytical determination of separation point. Perform Thwaites-Walz analysis using inviscid-ideal velocity profile and corrected velocity profile from Hiemenz flow (top surface).
 - d. Comments on the observation and differences observed in the results obtained from three approaches.
- 6. Plot the contours of vorticity magnitude and show the vortex shedding as shown in Fig. 17 (please refer the supplementary video on Canvas).
7. Explain why wall pressure is same as boundary layer edge pressure, when can this fail?
8. Estimate the edge velocity profile over cylinder using Bernoulli Principle (Eq.10). Compare this with ideal (Eq. 5) and Hiemenz fit (Eq. 20). Discuss the applicability. Up until which point can the edge velocity be estimated using Bernoulli Principle?
9. Can reduced order boundary layer analysis methods which decouples the inviscid and viscous phenomena be used directly for flow over bluff bodies? Reason your answer No

(EXTRA CREDIT)

Using the case file provided, setup the computational simulation with the inlet velocity 10 m/s. Determine the Reynolds number

- a. Refer the time step calculation in the supplementary video and determine an appropriate time step size for this simulation
- b. Determine the separation location as mentioned in steps 3 and 4 in the report requirements

VII. References

- [1] E. L. Houghton, P. W. C. *Aerodynamics for Engineering Students*. Butterworth-Heinemann, 2003.
- [2] Gerrard, J. H. “Flow around Circular Cylinders; Volume 1. Fundamentals. By M. M. Zdravkovich. Oxford Science Publications, 1997. 672 Pp. £120.” *Journal of Fluid Mechanics*, Vol. 350, 1997, pp. 375–378.
- [3] Roshko, A. “Perspectives on Bluff Body Aerodynamics.” *Journal of Wind Engineering and Industrial Aerodynamics*, Vol. 49, No. 1, 1993, pp. 79–100.
[https://doi.org/https://doi.org/10.1016/0167-6105\(93\)90007-B](https://doi.org/https://doi.org/10.1016/0167-6105(93)90007-B).
- [4] Coutanceau, M., and Defaye, J.-R. “Circular Cylinder Wake Configurations: A Flow Visualization Survey.” *Applied Mechanics Reviews*, Vol. 44, No. 6, 1991, pp. 255–305.
<https://doi.org/10.1115/1.3119504>.
- [5] Williamson, C. H. K. “Vortex Dynamics in the Cylinder Wake.” *Annual Review of Fluid Mechanics*, Vol. 28, No. 1, 1996, pp. 477–539.
<https://doi.org/10.1146/annurev.fl.28.010196.002401>.
- [6] White, F. M., and Majdalani, J. *Viscous Fluid Flow*. McGraw-Hill New York, 2006.
- [7] Niemann, H.-J., and Hölscher, N. “A Review of Recent Experiments on the Flow Past Circular Cylinders.” *Journal of Wind Engineering and Industrial Aerodynamics*, Vol. 33, No. 1, 1990, pp. 197–209. [https://doi.org/https://doi.org/10.1016/0167-6105\(90\)90035-B](https://doi.org/https://doi.org/10.1016/0167-6105(90)90035-B).
- [8] White, F. M. *Fluid Mechanics*. McGraw-Hill New York
- [9] Bertin, J. J., and Cummings, R. M. *Aerodynamics for Engineers*. Cambridge University Press, Cambridge, 2021.
- [10] Sucker, D., and Brauer, H. “Fluiddynamik Bei Quer Angeströmten Zylindern.” *Wärme- und Stoffübertragung*, Vol. 8, No. 3, 1975, pp. 149–158.
- [11] Allen, H. J., and Vincenti, W. G. “Wall Interference in a Two-Dimensional-Flow Wind Tunnel, With Consideration of the Effect of Compressibility.” *Annual Report of the National Advisory Committee for Aeronautics*, Vol. 268, 1949, p. 155.

Abstract: 3 pts

Introduction: 10 pts

Experimental procedure: 10 pts.

Post-processing in results and discussion: 65 pts

Comparison: 10-15 pts.

Conclusion: 10 pts (key numerical data: what is happening, numerical have and explain how we did it in 1 sentence).

What possible errors in the experiment - conclusion.

References: 2 pts.

Extra credit: ?? pts.